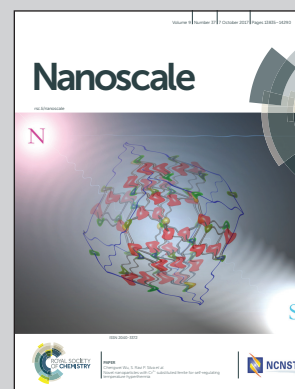


Showcasing research from the Department of Condensed Matter Physics, Universidad Autónoma de Madrid, and the Department of Nanostructures and Surfaces, Institute of Material Science, CSIC, Madrid.

Mapping stress in polycrystals with sub-10 nm spatial resolution

Sensing stress in polycrystals through the stress stiffening effect using atomic force microscopy techniques. This effect, that resembles the behavior of a membrane, allows for the mapping of stress in polycrystalline films with sub-10 nm spatial resolution. In this way, we enlarge the catalogue of mechanical properties of stiff materials that can be characterized at nanoscale by AFM techniques.

As featured in:

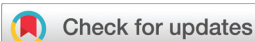


See C. Polop et al., *Nanoscale*, 2017, 9, 13938.



rsc.li/nanoscale

Registered charity number: 207890



Cite this: *Nanoscale*, 2017, 9, 13938

Mapping stress in polycrystals with sub-10 nm spatial resolution†

C. Polop, *^a E. Vasco,^b A. P. Perrino^b and R. Garcia ^b

From aircraft to electronic devices, and even in Formula One cars, stress is the main cause of degraded material performance and mechanical failure in applications incorporating thin films and coatings. Over the last two decades, the scientific community has searched for the mechanisms responsible for stress generation in films, with no consensus in sight. The main difficulty is that most current models of stress generation, while atomistic in nature, are based on macroscopic measurements. Here, we demonstrate a novel method for mapping the stress at the surface of polycrystals with sub-10 nm spatial resolution. This method consists of transforming elastic modulus maps measured by atomic force microscopy techniques into stress maps *via* the local stress-stiffening effect. The validity of this approach is supported by finite element modeling simulations. Our study reveals a strongly heterogeneous distribution of intrinsic stress in polycrystalline Au films, with gradients as high as 100 MPa nm⁻¹ near the grain boundaries. Consequently, our study discloses the limited capacity of macroscopic stress assessments and standard tests to discriminate among models, and the great potential of nanometer-scale stress mapping.

Received 3rd February 2017,

Accepted 9th June 2017

DOI: 10.1039/c7nr00800g

rsc.li/nanoscale

Introduction

The intrinsic stress σ generated during the preparation and processing of polycrystalline solids is a persistent problem and common source of failure in present-day technology. This stress originates from imperfections such as lattice defects, interfaces and free surfaces, and significantly reduces material performance. Polycrystalline coatings are particularly susceptible because their shapes with high surface-to-bulk ratios are mechanically stabilized by moderated cohesion and adhesion forces. Intrinsic stress in the order of those forces can cause mechanical failures such as film fracture, delamination/peel-off, crack propagation, and premature thermo-mechanical fatigue.^{1–4}

Three features make intrinsic stress particularly harmful for these systems. (i) It is unavoidable: even a single-crystal solid has non-zero defect density in its lattice due to entropy under conditions of thermodynamic equilibrium. The defect density is higher in films due to kinetic limitations caused by the deposition conditions and substrate constraints. (ii) It is reversible and cumulative: intrinsic stress can be regenerated

by residual stress in the system (the unreleased fraction under normal temperature and pressure – NTP), and can accumulate under conditions of heating, overpressure, and periodic loads. (iii) It exhibits a non-uniform spatial distribution at the scale of the solid lattice defects. In polycrystals, this scale (~10–100 nm) is far below the resolution of standard stress tests. Macroscopic assessments are ineffective at detecting these steep stress gradients, which can be higher than the mechanical strengths required for commercial use (including safety margins). Consequently, stress mapping at the nanoscale is an irreplaceable tool for the study of material resistance and nanomechanics.

The failure of current technology to investigate stress at the inherent spatial scales of polycrystals is mirrored in the academic world, where the mechanisms responsible for stress generation during film deposition and processing have generated intense conjecture and scientific activity.^{5–12} However, no consensus has been reached so far. The main difficulty is that current models of stress generation, most of which are atomistic in nature, are only supported by data with, at best, sub-micron resolutions. For example, techniques such as curvature-based measurements, Raman spectroscopy, and X-ray diffraction cannot reveal the stress distribution in films on nanometer scales.

Atomic force microscopy (AFM) is a suitable tool for determining the mechanical properties of solids at the nanoscale.^{13–15} In this work, we develop a method to map the stress on the surface of polycrystals with sub-10 nm spatial resolution. Our method maps the elastic modulus of the

^aDepartamento de Física de la Materia Condensada and Instituto Nicolás Cabrera, Universidad Autónoma de Madrid, 28049 Madrid, Spain.

E-mail: celia.polop@uam.es

^bInstituto de Ciencia de Materiales de Madrid, CSIC, Sor Juana Inés de la Cruz 3, 28049 Madrid, Spain

†Electronic supplementary information (ESI) available. See DOI: 10.1039/c7nr00800g

surface by two AFM techniques (Force Modulation Microscopy and bimodal AFM), then transforms these data into a stress map *via* the local stress-stiffening effect. The validity of our method is supported by Finite Element Modeling (FEM) simulations. Applying this method to Au films reveals a highly heterogeneous distribution of intrinsic stress along grain diameters, with stress gradients as high as 100 MPa nm⁻¹ near the grain boundaries (GBs). Consequently, our results call into question the validity of stress assessments based on standard tests and micrometer-scale characterization techniques.

Results and discussion

Elastic modulus maps

As a benchmark for the application of force modulation microscopy (FMM) on materials with low stiffness contrast, we first studied isolated Cu grains evaporated on Si(100) substrates (Fig. 1). Fig. 1a and b show simultaneously taken topography and FMM amplitude images, respectively, of several Cu grains. The profiles (Fig. 1c) are measured along the dashed-blue and continuous-red lines plotted in the images. In this example, the Cu grains are about 20 nm in diameter and 2 nm high. The cantilever vibration amplitude A_{FMM} is lower over the Cu grains than over Si, consistent with the fact that Cu has a lower Young's modulus ($E_{\text{Cu}} = 130$ GPa while $E_{\text{Si}} = 170$ GPa). This FMM amplitude contrast is consistent for all modulation frequencies $f < 0.7f_{01}$, where f_{01} is the resonance frequency of the first mode of the cantilever. The fact that we can observe variations in A_{FMM} as small as 0.2 Å, due solely to minute differences in the indentation amplitudes Δd , demonstrates both the high sensitivity of FMM and its suitability for

imaging systems with low stiffness contrasts (see the Methods section for details).

Fig. 2 shows the results of the FMM experiments measured at dissimilar modulation voltage ΔV on Au films with two different thicknesses: 600 nm in (a, c, e) and 1200 nm in (b, d, f, g, h). For each experiment, we try three different modulation voltages ΔV driving the probe vibration. The Methods section describes how we estimate the corresponding force modulation ΔF . Comparing the topography of both films (Fig. 2a and b), we see that grain size increases with film thickness as expected (note the different length scales). The grains with flat tops are surrounded by deeper regions where GBs intercept the surface.¹⁶ The overlapping height distributions for different values of ΔV (the histograms of Fig. 2a and b) demonstrate that the topography measurements are independent of ΔF , and hence that the average tip-sample contact geometry is preserved.

Fig. 2c and d show the corresponding FMM amplitude maps, together with their A_{stiff} -normalized histograms. The meaning of A_{stiff} is discussed below. In general, we observed only slight variations in A_{FMM} within grains (light areas). However, the amplitude A_{FMM} decreases dramatically near the GBs (dark areas) and peaks inside the GBs (white areas). The FMM amplitude images also reveal some small-scale morphological features such as vicinal surfaces (arrows in Fig. 2c and d) with better resolution than the topography images. A possible explanation for this enhanced FMM resolution is provided in the Methods section.

Once the FMM amplitude was measured, we mapped the effective elastic modulus E_{eff} using the following novel procedure. For an FMM probe excited by a piezoelectric actuator coupled to the cantilever base, the A_{FMM} response is described by the equation:^{17–21}

$$\frac{A_{\text{FMM}}}{A_{\text{stiff}}} = \frac{k_{\text{eff}}}{k_1 + k_{\text{eff}}} \quad (1)$$

where A_{stiff} is the amplitude of the cantilever vibration on an infinitely stiff sample, k_1 is the force constant of the first mode of the cantilever, and k_{eff} denotes the effective force constant of the tip-sample contact. k_{eff} is defined by a Taylor expansion of the Hertz equation:

$$k_{\text{eff}} = [6F_L E_{\text{eff}}^2 R_{\text{eff}}]^{1/3} \quad (2)$$

where F_L is the static load, $E_{\text{eff}} = [(1 - \nu_{\text{tip}}^2)/E_{\text{tip}} + (1 - \nu_{\text{sample}}^2)/E_{\text{sample}}]^{-1}$ is the effective elastic modulus taking into account deformations of both the tip and sample (ν_x is the Poisson ratio of each material), and $R_{\text{eff}} = [1/R_{\text{tip}} + \kappa(\vec{r})]^{-1}$ is the effective radius of contact expressing the competition between the tip radius R_{tip} and the local curvature $\kappa(\vec{r})$ of the sample.²² To estimate A_{stiff} , we can either measure a reference FMM amplitude on a much stiffer sample or measure the amplitude on a region whose E_{sample} is known exactly. Since the samples are mostly relaxed at NTP, as measured by a multi-beam optical stress sensor (MOSS, see the ESI†), we use the latter method and assume that $E_{\text{sample}} = E_{\text{Au}} = 78$ GPa on the flat regions interior to the grains (the light areas in Fig. 2c and d).

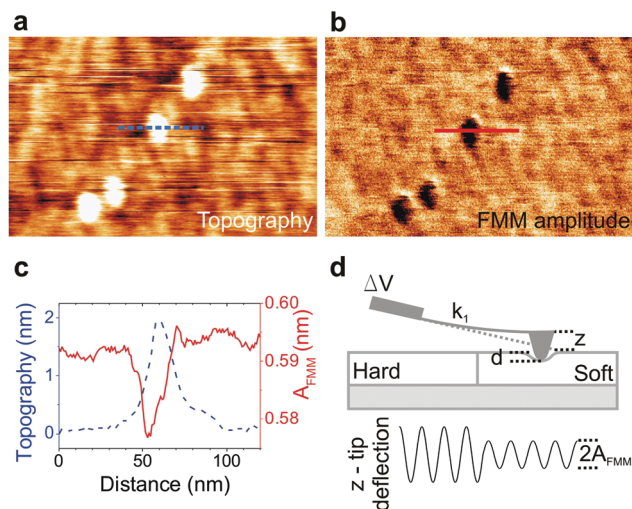


Fig. 1 Working principle of FMM in systems with low mechanical contrast. Simultaneously taken topography (a) and FMM amplitude (b) images of isolated Cu grains deposited on Si(100). (c) Topography and FMM amplitude profiles across the lines marked in (a) and (b). (d) Schematic of the FMM setup (see the Methods section).

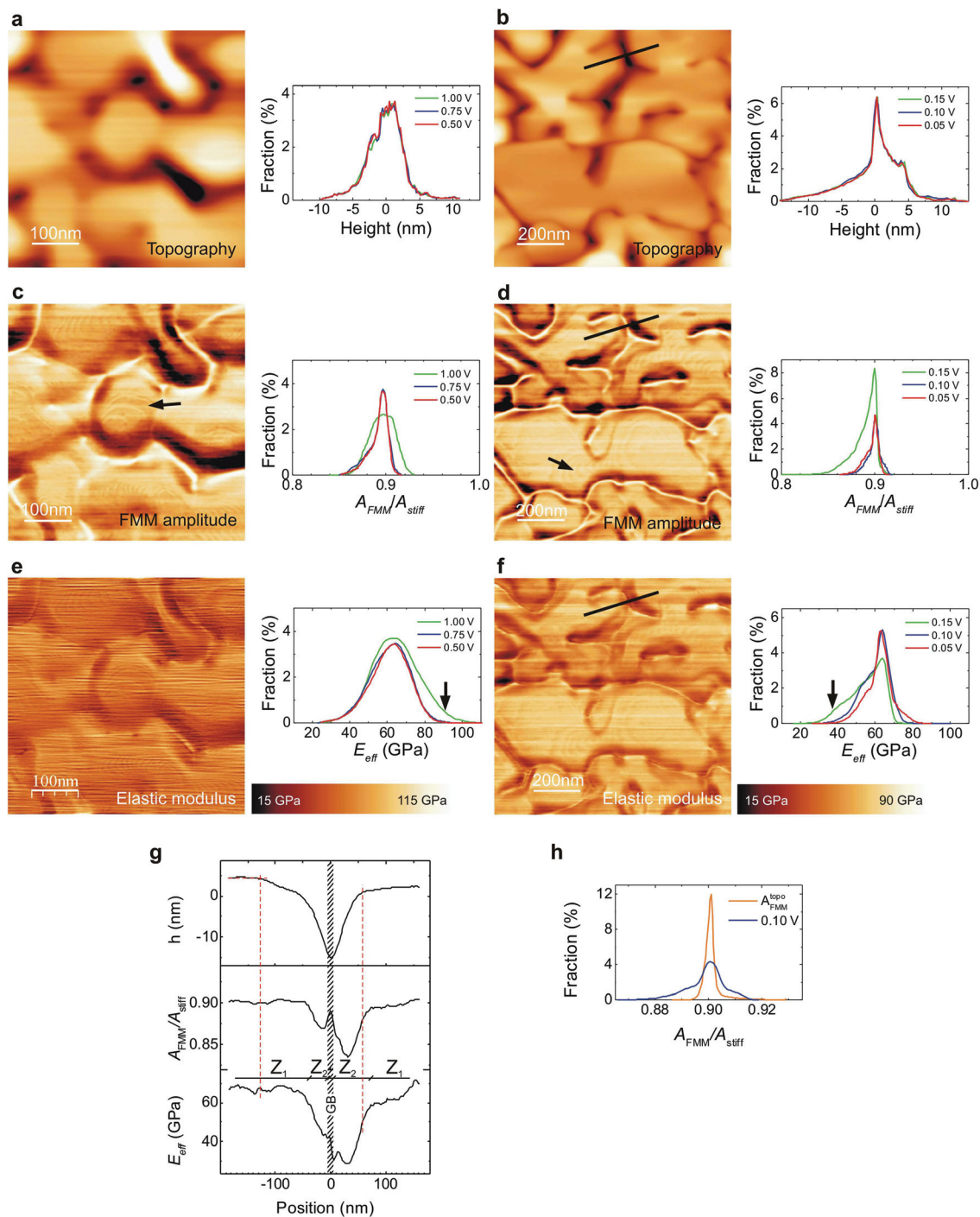


Fig. 2 Mechanical characterization at the nanoscale by FMM. The panels (a, c, e) and (b, d, f, g, h) correspond to 600 nm and 1200 nm thick Au films, respectively. The images are shown alongside histograms for the different ΔV . Panels (a, b), (c, d) and (e, f) correspond to the topography, FMM amplitude, and effective elastic modulus, respectively. The conversion of ΔV into force modulation ΔF is described in the Methods section. The FMM amplitude images in (c, d) correspond to those acquired at $\Delta V = 0.75$ V (with $F_L = 180$ nN and $f = 47$ kHz) and $\Delta V = 0.10$ V (with $F_L = 200$ nN and $f = 80.6$ kHz), respectively. The arrows in (c, d) point out vicinal structures, while those in (e, f) indicate abnormal broadening of the E_{eff} histograms. Panel (g) plots characteristic profiles of the mapped magnitudes along the lines depicted in (b, d, f). Dashed red lines identify the positions of topography slope changes and labels Z_i indicate regions with different mechanical behaviors as described in the text. Panel (h) shows a comparison of the histogram of the FMM amplitude map in (d) with that calculated from considering only the topography contribution A_{FMM}^{topo} to such a map. A_{FMM}^{topo} is calculated from the topography imaged in (b) assuming $E_{eff}(\vec{r}) = E_{eff}^{bulk}$.

Such regions comprise the majority of the imaged morphological features by area, corresponding to the *mode* of the A_{FMM} histograms, $\text{mode}(A_{\text{FMM}})$. Consequently, in these regions, the effective elastic modulus is $E_{\text{eff}}^{\text{bulk}} = [(1 - \nu_{\text{tip}}^2)/E_{\text{tip}} + (1 - \nu_{\text{Au}}^2)/E_{\text{Au}}]^{-1} \approx 63$ GPa, the effective radius is $R_{\text{eff}} = R_{\text{tip}}$, and the effective force constant is $k_{\text{eff}}^{\text{flat, surface}} = [6F_{\text{L}}(E_{\text{eff}}^{\text{bulk}})^2 R_{\text{tip}}]^{1/3}$. Eqn (1) then becomes $A_{\text{stiff}} \approx (1 + k_1/k_{\text{eff}}^{\text{flat, surface}}) \cdot \text{mode}(A_{\text{FMM}})$, which allows us to estimate an *in situ* value for A_{stiff} . We discarded the alternative approach, where A_{stiff} is measured on a much stiffer sample, because swapping samples would create unavoidable changes in the experiment geometry.

At this point, we need to remove the topography contribution from the FMM amplitude maps, because the rough surface of the samples has an impact on the FMM amplitude images (by changing the contact area of the probe). If we assume that the intrinsic mechanical properties of the sample are independent of its morphology (*i.e.*, we reject potential finite-size effects), the spatial dependence of E_{eff} can be described as a perturbation $E'(\vec{r})$ around its bulk value $E_{\text{eff}}^{\text{bulk}}$, thus $E_{\text{eff}}(\vec{r}) = E_{\text{eff}}^{\text{bulk}} E'(\vec{r})$. By substituting this form of $E_{\text{eff}}(\vec{r})$ into eqn (2), we can express k_{eff} in terms of separable functions:

$k_{\text{eff}}(\vec{r}) = k_{\text{eff}}^{\text{topo}}(\vec{r}) \times E'(\vec{r})^{2/3}$. Here, $k_{\text{eff}}^{\text{topo}}(\vec{r}) = [6F_{\text{L}}(E_{\text{eff}}^{\text{bulk}})^2 R_{\text{eff}}(\vec{r})]^{1/3}$ describes exclusively the morphology dependence of k_{eff} due to the local curvature $\kappa(\vec{r})$ of the surface. Thus, the effective elastic modulus at each point on the image is calculated as follows:

$$E_{\text{eff}}(\vec{r}) = E_{\text{eff}}^{\text{bulk}} [k_{\text{eff}}(\vec{r})/k_{\text{eff}}^{\text{topo}}(\vec{r})]^{3/2} \quad (3)$$

where $k_{\text{eff}}(\vec{r})$ is computed by eqn (1) from the FMM amplitudes (raw FMM data) and $k_{\text{eff}}^{\text{topo}}(\vec{r})$ is calculated from the simultaneously measured topography (see above).

Fig. 2e and f show the E_{eff} maps for the Au samples together with their histograms. Fig. 2g plots typical profiles across a GB for the three mapped magnitudes (topography, A_{FMM} and E_{eff}). The profile paths are the solid straight lines overlaid on the maps. The E_{eff} maps reveal that the inner grain regions do have homogeneous mechanical properties, with E_{eff} variations being no more than 10% (region Z_1 in Fig. 2g). The regions near a GB are softer than the grain interior, with E_{eff} decreasing to 48% of $E_{\text{eff}}^{\text{bulk}}$ (region Z_2). The values of E_{eff} inside the GBs (where A_{FMM} peaks) are influenced by the difficulty of accessing these narrow gaps with the probe tip and we do not analyze them. The decrease in E_{eff} near the GBs is significant and reproducible for different R_{tip} (we used both standard and ultrasharp tips, with nominal $R_{\text{tip}} = 10$ and 2 nm) and different scanning angles.

Examining Fig. 2g, we see that the A_{FMM} and E_{eff} profiles (middle and bottom panels) do not follow the shape of the height profile (top) around the GB. In particular, the positions where the topography slope changes (marked by red dashed lines) do not coincide with major variations in A_{FMM} . The fact that both profiles are scanned simultaneously rules out the possibility that this shift is caused by potential artifacts of measurement or topography. Additionally, we calculated the normalized topography contribution to the FMM amplitude,

$A_{\text{FMM}}^{\text{topo}} = k_{\text{eff}}^{\text{topo}}/(k_1 + k_{\text{eff}}^{\text{topo}})$, and compared it with the experimental A_{FMM} maps. The corresponding histograms are shown in Fig. 2h. The degree of overlap between the histograms indicates the amount of contrast in the A_{FMM} maps that originates from topography effects. If the majority of the A_{FMM} contrast is due to topography, we would also obtain flat E_{eff} maps (fixed to the value $E_{\text{eff}}^{\text{bulk}}$) after removing the topography contribution. Fig. 2h reveals that the hypothesis fails: the A_{FMM} histogram is significantly wider and preferentially spread to lower (*i.e.*, softer) values. The following conclusions can be drawn: (i) the topography contribution predicts a more homogeneous mechanical response than what we actually measured; and (ii) the surface measured by FMM is more compliant than expected from the topography contribution alone. Consequently, we can conclude that topography plays a minor role in the contrast of the A_{FMM} maps, which is removed in the E_{eff} maps.

Increasing ΔV beyond a certain threshold, which is defined by the condition $\Delta F > F_{\text{L}}/2$, causes an abnormal broadening of the E_{eff} histograms (see arrows in Fig. 2e and f). We know that this broadening is not related to changes in the average contact geometry, such as tip deformation or plastic regime, because those would also be visible in the topographic images (note that the height histograms still overlap). Two possible explanations for the histogram broadening are anharmonic distortions in the mechanical response of the sample¹⁷ (probably responsible for the high- E_{eff} tail in the histogram of Fig. 2e) and/or small slips of the tip on steep regions¹⁸ (the low- E_{eff} tail in the histogram of Fig. 2f).

To validate our method, Fig. 3 compares the inferred E_{eff} results obtained by FMM (b) with E_{eff} maps obtained independently by bimodal AFM (a), for different regions of the 1200 nm thick Au film. The latter method determines the effective elastic modulus without any prior assumptions.^{23–26}

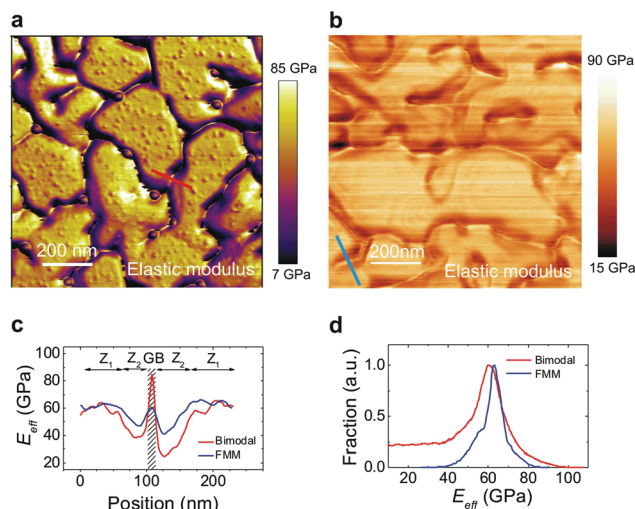


Fig. 3 Comparison of bimodal AFM (a) and FMM (b) maps of the elastic modulus, taken from the different regions of the same 1200 nm thick Au film. (c) Comparison between the E_{eff} profiles along the red and blue lines plotted in (a, b). (d) Comparison of the corresponding E_{eff} histograms.

The general features of the E_{eff} maps obtained by both techniques agree with regard to: (i) the low dispersion of mechanical properties within the grain interiors ($E_{\text{eff}} \approx E_{\text{eff}}^{\text{bulk}} \pm 6\%$ for bimodal AFM), (ii) the fact that regions close to a GB are softer (E_{eff} decreases to 42% of $E_{\text{eff}}^{\text{bulk}}$ in the bimodal AFM map) and (iii) the observed peak in E_{eff} at the GBs. This qualitative agreement between the three types of regions and their behaviors is supported by the two GB-crossing profiles depicted in Fig. 3c. Fig. 3d compares the corresponding E_{eff} histograms. The difference in the *modes*, which are 60 GPa and 63 GPa for bimodal AFM and FMM, respectively, is within the error generated during calibration of the cantilever force constants. The good agreement between the results obtained by the two different AFM techniques with dissimilar tip-sample interactions (while the FMM requires a strong continuous contact, the bimodal AFM is based on weaker intermittent contact), using two different setups (see the Methods section) supports our proposed procedure for E_{eff} mapping by FMM experiments on stiff polycrystalline films.

Stress maps

The fact that the elastic modulus E_{sample} is a cooperative lattice property allows us to correlate its variation at the nanoscale with the strain field in a solid. The macroscopic elastic modulus of a material is highly sensitive to massive defects²⁷ such as voids, incohesive grain bonds, and the inclusion of non-crystallized particles. In contrast, microscopic E_{sample} varies only by a few percent even in the presence of major deformations, dramatic atomic rearrangements, and intense fields of intrinsic stress. This is because the lattice of a crystalline solid admits only small perturbations. For example, the lattice anharmonicity effect in fcc-metal films changes the microscopic E_{sample} by less than 5% for equibiaxial intrinsic stresses as high as $\sigma_i = \pm 1$ GPa.²⁷ However, the E_{eff} maps in Fig. 2 and 3 involve spatial variations of 20–50%. This is much higher than expected, and also higher than the intrinsic E_{sample} values measured by contactless (optical) techniques. Large variations in microscopic E_{sample} have only previously been reported in Au–Ni and Cu–Pd multilayers with composition modulation wavelengths lower than 3 nm (supermodulus effect).²⁸ Conversely, in our study, large variations in E_{sample} are observed on the free surfaces of films with submicrometer thicknesses.

The high variability of E_{eff} observed in our study suggests that the elastic moduli measured by FMM and bimodal AFM are affected by the tip-sample contact (note that this does not happen with optical techniques). In this case, the spatial variation in E_{sample} is mostly due to a stress-stiffening effect (also known as geometric nonlinearity). This process is typical of stressed membranes when the deformation produced by a normal load generates out-of-plane contributions of the stress force that counteract such a load. In our case, the membrane corresponds to the outermost sublayer of the film, the normal load is F_L , the out-of-plane deformation is the indentation depth d (as defined by the Hertz model), and the stress in the membrane corresponds to the biaxial intrinsic stress in the

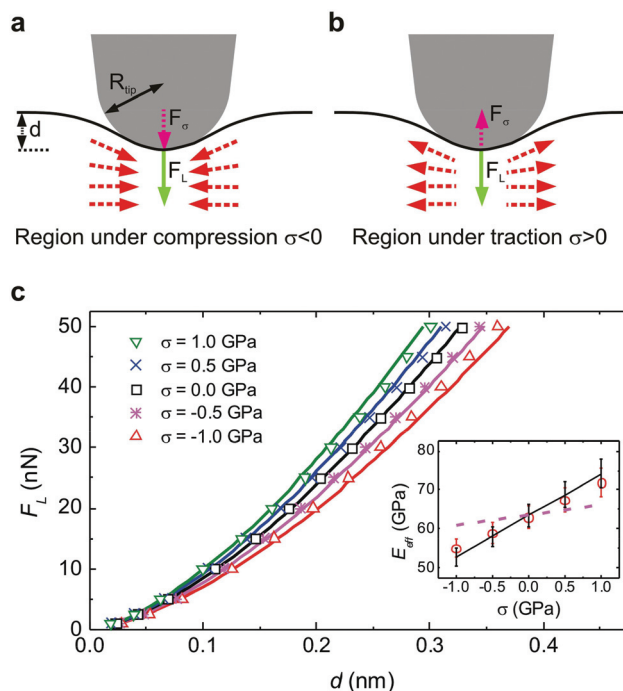


Fig. 4 Stress-stiffening effect. (a, b) Diagrams of the tip–film contact geometry in regions under stress of compression and traction respectively, showing the parameters of the stress-stiffening model. (c) Load-indentation curves computed by FEM (symbols) and by the stress-stiffening model (continuous lines) for σ -stressed isotropic Au films under a load exerted by a Si tip.²⁹ The inset shows the σ -dependencies of E_{eff} computed from the fit of the FEM results to the updated Hertz model (symbols), the stress-stiffening model (solid line), and the lattice anharmonicity effect estimated for Au <111> films (dashed curve).³⁰

film σ . Thus, as sketched in Fig. 4a and b, the indentation of a region under compression (with $\sigma < 0$, dashed red arrows) creates a stress force F_σ that strengthens F_L . On the other hand, the indentation of a region under traction ($\sigma > 0$) creates a stress force F_σ that counters F_L . The fact that we calculate E_{eff} from F_L instead of $F_L \pm F_\sigma$ implies an underestimation (overestimation) of the applied load, and means that the regions under compression (traction) are displayed as softer (stiffer): *i.e.*, $E_{\text{eff}} < E_{\text{eff}}^{\text{bulk}}$ ($E_{\text{eff}} > E_{\text{eff}}^{\text{bulk}}$).

Fig. 4c (symbols) shows the load-indentation curves computed by FEM for σ -stressed isotropic Au films under a normal load F_L exerted by a Si tip.²⁹ The curves for different values of σ follow a power law of the form $F_L \propto d^{1.5 \pm 0.1}$, in agreement with the Hertz model. As previously discussed, the indentation depth for a given F_L increases as σ decreases (considering the sign). The σ -dependence of E_{eff} is calculated by fitting each curve to the Hertz model. This dependence is plotted in the inset of Fig. 4c (symbols), together with the E_{eff} variations due to changing σ expected from the lattice anharmonicity effect in Au(111) films³⁰ (dashed curve). The FEM results show a stronger σ -dependence (*e.g.*, E_{eff} changes up to 20% for $\sigma \leq \pm 1$ GPa) than that estimated for the lattice anharmonicity effect, which predicts changes in E_{eff} only up to 4%. Consequently, the E_{eff} variation with σ found by FEM appears to be consistent with

the spatial dispersions in the E_{eff} maps (Fig. 2 and 3), since local residual stress σ of at most a few GPa is expected. It should be remembered that the Au films are macroscopically relaxed (as measured by MOSS, see the ESI†). Therefore, the stresses causing the E_{eff} dispersion correspond to local residual fractions of the growth intrinsic stress that survives at NTP.

By taking into account the σ -dependence of E_{eff} found by FEM, we can now transform the E_{eff} maps into σ maps using the following analytical model of stress stiffening. The film indentation caused by the tip pressure breaks the in-plane film symmetry. The biaxial intrinsic stress σ in the film therefore contributes an amount $P_\sigma = \beta(\sigma \cdot \hat{z})$ to the normal pressure, where β is a factor describing the stress field geometry³¹ and \hat{z} is the unit vector normal to the film plane. This contribution can be estimated as $(\sigma \cdot \hat{z}) \approx \sigma \cos[\arctan(2\sqrt{R_{\text{tip}}/d})]$, where $\sqrt{R_{\text{tip}}d}$ is the radius of the contact surface A (shaped like a spherical cap). P_σ generates a stress force on the tip:

$$F_\sigma = A \cdot P_\sigma = \pi R_{\text{tip}} d \cdot \beta \sigma \cos\left[\arctan\left(2\sqrt{R_{\text{tip}}/d}\right)\right] \quad (4)$$

Hence, the resulting force becomes $F_T = F_L - F_\sigma$. Updating the Hertz model to take stress stiffening into consideration, we obtain $F_T = \frac{4}{3} E_{\text{eff}}^{\text{bulk}} R_{\text{eff}}^{1/2} d^{3/2}$. Now, if we interpret the spatial F_T variation due to the stress field $F_\sigma(\vec{r}) \propto \sigma(\vec{r})$ in terms of the E_{eff} variation, we get:

$$\Delta E_{\text{eff}}(\sigma) = E_{\text{eff}}(\sigma) - E_{\text{eff}}^{\text{bulk}} = E_{\text{eff}}^{\text{bulk}} \frac{F_\sigma}{F_L - F_\sigma} \quad (5)$$

where $E_{\text{eff}}(\sigma = 0) = E_{\text{eff}}^{\text{bulk}}$. From eqn (4) and (5), the regions under compression ($\sigma < 0 \rightarrow F_\sigma < 0$) seem to be softer ($\Delta E_{\text{eff}} < 0$) than they really are, while those under traction ($\sigma > 0 \rightarrow F_\sigma > 0$) seem to be stiffer ($\Delta E_{\text{eff}} > 0$). The continuous lines in Fig. 4c and its inset show the load-indentation curves and the σ -dependence of E_{eff} obtained from our analytical model. The good agreement between our model and the FEM simulations (the model overestimates ΔE_{eff} by 2–3%) supports the key role played by stress stiffening in the measured E_{eff} dispersion.

Eqn (5) allows us to transform the E_{eff} maps into $F_\sigma(\vec{r})$. Then, by substituting F_σ into the updated Hertz model, we can compute the σ maps shown in Fig. 5a and b for the 600 nm and 1200 nm thick Au films, respectively. Since the σ contribution to F_σ (eqn (4)) depends on the indentation depth, deeper indentations induced by higher force modulations ΔF of the tip load are required to sense lower stresses. However, increasing ΔF beyond a certain threshold also produces abnormal broadening of the E_{eff} histograms, as discussed above. Thus, the practical ΔF maximum determines the amount of uncertainty in the stress resolution $\delta\sigma$. This uncertainty is defined as the minimum σ variation required to produce a change in d greater than the experimental error in determining the indentation depth δd (see the Methods section).

Because the intrinsic stress modifies the indentation depth nonlinearly, the analytical model determines a series of uncertainties $\delta\sigma_i$ for different measurement ranges. The uncertainty varies with both the sign and the magnitude of the intrinsic

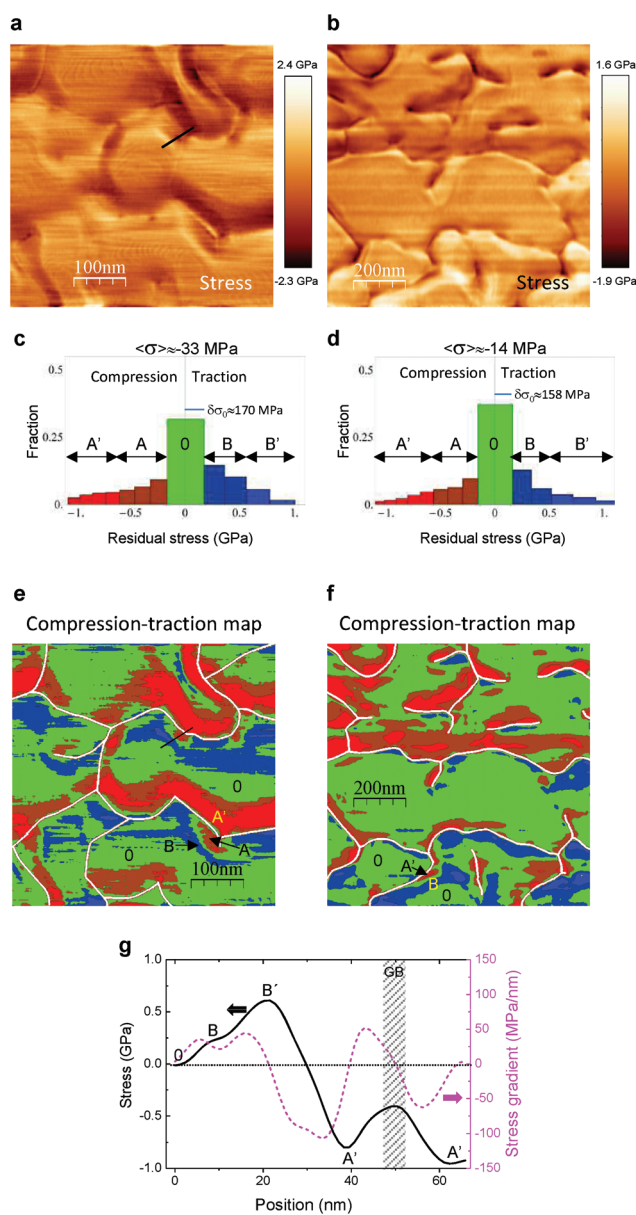


Fig. 5 Residual stress (σ) maps on the nanoscale. (a, b) σ maps of 600 nm and 1200 nm thick Au films, calculated from FMM images obtained at $\Delta V = 0.75$ V and 0.10 V, respectively. (c, d) Histograms identifying the major stress levels in the two films, namely: relaxed regions (0, green), areas under low and high compression (A and A', dark and light red), areas under low and high traction (B and B', dark and light blue). $\langle\sigma\rangle$ averaged over each map is reported above the corresponding histogram together with the σ uncertainties around the relaxed state $\delta\sigma_\sigma$. Note that $\delta\sigma_i$ (width of the histogram bins) depends on both the sign and the magnitude of σ as described in the text. (e, f) Compression–traction maps of the Au films, using the discrete color scale defined in the histograms (c) and (d). (g) Stress profile (continuous black line) along the line plotted in (a) and its corresponding 1D gradient (dashed magenta line referred to the right axes).

stress. These uncertainties are used to determine the statistical properties of the σ maps, and correspond to the bin widths of the histograms in Fig. 5c and d. As specified in the histograms, the intrinsic stress measurements are grouped into five

levels (colors): 0-green, A-dark red, A'-light red, B-dark blue and B'-light blue. The green bins represent the relaxed area, while the red (blue) bins collect measurements from areas under compression (traction). Dark (light) colors correspond to the areas under low (high) stress. Fig. 5e and f redraw the σ maps using this discrete color scale, to improve the contrast between regions with different stress levels. In addition, these figures illustrate the GB mesh with white lines, calculated by applying a tessellation filter to the topography images.³² The line thickness in the figure is similar to the diameter of the tip-sample contact area (≈ 5.5 – 5.7 nm), providing a visual estimation of the areas inaccessible to the AFM tip. We call this simplified representation a “compression–traction map” hereafter.

Typical values of $\delta\sigma_i$ obtained under our experimental conditions are a few hundred MPa. For example, the average uncertainties in the σ maps around the relaxed state (level 0) in Fig. 5a and b are $\delta\sigma_0 \approx 170$ and 158 MPa, respectively. This stress uncertainty also reduces the spatial (lateral) resolution of the σ maps. The spatial resolution is theoretically limited by the diameter of the contact area ($2\sqrt{R_{\text{tip}}d} \approx 5.5$ – 5.7 nm for both maps), but worsens to $\delta\sigma_i/\nabla\sigma$ where $\nabla\sigma$ is the magnitude of the stress gradient to be resolved. For example, given the statistics of the σ maps in Fig. 5a and b, we can estimate their average stress gradients as $\langle\nabla\sigma\rangle = 26.6$ and 25.8 MPa nm⁻¹, respectively. This implies that the maps have average spatial resolutions of $\delta\sigma_0/\langle\nabla\sigma\rangle \approx 6.4$ and 6.1 nm, respectively. Since these resolutions (below 10 nm) are smaller than the inherent length scales of the lattice imperfections in polycrystals (~ 10 – 100 nm), the method of stress mapping proposed here is good enough to image residual stress gradients in polycrystalline films. In particular, the method is suitable to sense the stress within the outermost sublayer with thickness in the order of the indentation depth d (~ 1 nm for F_L of a few hundred nN). Note that this sublayer plays a key role in the mechanical properties of systems with a high surface-to-volume ratio.

The compression–traction maps reveal that the stress distribution in polycrystals is highly heterogeneous: relaxed areas alternate with regions under compression and traction. Some regions exemplifying the different stress regimes are highlighted in Fig. 5e and f. While the inner vicinal surfaces of the grains are mostly relaxed (0-green areas), most of the regions near the grain boundaries are under compression (A and A'-red areas). Annular areas with traction stress (B-blue areas) appear frequently in between the previous two regions. Fig. 5g shows a typical stress profile measured across a GB, performed along the black line in Fig. 5a. The corresponding 1D gradient (right axis) demonstrates that residual stress gradients as high as 100 MPa nm⁻¹ persist along the grain diameters in macroscopically relaxed films.

These results are directly connected to the generation of compressive stress at the post-coalescence stage (*i.e.*, once the GBs are formed) during the deposition of polycrystalline films, which is extensively discussed in the literature.^{5–12} Although we are mapping residual stresses rather than *in situ* growth stresses, it is reasonable to assume that the two quantities are related in a straightforward way by stress-relaxation thermo-

dynamics. Thus, after deposition stops, the accumulated growth stress relaxes progressively until it reaches a steady state (residual stress), wherein the strain energy generated by the residual stress is lower than the activation energy of the relaxation mechanism. Subsequently, two preliminary conclusions can be drawn from our results. (i) Neither force–dipole interactions between morphology features⁵ nor adatom insertion between ledges⁶ at vicinal surfaces are responsible for post-coalescence compression, since those areas are mostly relaxed. (ii) The fact that compression regions mostly decorate GB edges indicates that GBs are involved in the generation of the post-coalescence compression, as proposed in ref. 7, 10 and 12. We will address the physical origin of the stress gradients along the grain diameter in a forthcoming work.

Finally, note that the heterogeneous distribution of stress over the surface of polycrystalline films, as resolved here in the sub-10 nm stress maps, is undetectable by the standard techniques and tests used for stress analysis. Such techniques, which have sub-micron spatial resolutions at best, are only sensitive to the average stress over the entire displayed areas in Fig. 5a and b: $\langle\sigma\rangle \approx -33$ MPa and -14 MPa, respectively. Besides, these values correspond to the macroscopically relaxed samples, as discussed above. Furthermore, average stresses hide the existence of steep gradients (as high as 100 MPa nm⁻¹ in Au) which can be greater than the mechanical strengths required by many applications.³³ Consequently, we hope that stress mapping at the nanoscale becomes an irreplaceable tool for the study of material resistance. More generally, this and other nanomechanical technologies will change our perception about the atomistic nature of stress in crystalline solids.

Conclusions

We have presented a method to map mechanical stresses on the surface of polycrystals with sub-10 nm spatial resolution. The method directly observes spatial variations in the elastic properties of a crystalline solid over its surface, in particular, the elastic modulus maps provided by AFM techniques. We transform these values into stress maps using an analytical model of stress-stiffening. The consistency of this model is supported by FEM simulations. The application of this method to the study of evaporated Au films up to 1 micron in thickness reveals a strongly heterogeneous distribution of the intrinsic stress, with gradients as high as 100 MPa nm⁻¹ along the grain diameters. Such extreme values, which occur near grain boundaries, could compromise the mechanical reliability of polycrystalline films in many applications.

Methods

Sample preparation

The Au films were deposited by thermal evaporation on mica substrates at room temperature. Films with thicknesses within

the range of 200–1200 nm were grown at 0.1 nm s^{-1} under a pressure of 10^{-7} mbar. The samples were *ex situ* characterized by scanning electron microscopy, X-ray diffraction and AFM microscopy. All the films exhibited a [111]-textured columnar microstructure without in-plane order (see the ESI†).

Force modulation microscopy

Background. FMM (also called ‘modulated nanoindentation’³⁴) is an AFM technique used to study materials with intermediate stiffness ($1 \text{ GPa} < E_{\text{sample}} < \text{hundreds of GPa}$). Using a standard AFM set-up, FMM measures the amplitude of vibration in a cantilever whose tip is held in continuous contact with the surface of the sample (see Fig. 1d). As it moves across the surface, the cantilever vibrates at a frequency f lower than its first resonance f_{01} .^{17–21,34} This vibration is induced by applying a modulation voltage ΔV to a piezoelectric element at the base of the cantilever or the sample (acoustic excitation). This process results in a load modulation ΔF around the static load F_L used to hold the continuous contact. The amplitude of the cantilever vibration A_{FMM} is measured by a four-sector photodiode operating in a frequency-locked loop (FLL). Relatively high static load values ($F_L \sim \text{several hundred nN}$) are required to ensure that adhesion forces can be ruled out. The Hertz model predicts $F_L = \frac{4}{3} E_{\text{eff}} R_{\text{eff}}^{1/2} d^{3/2}$ for a spherical tip. From a Taylor expansion of the Hertz model for small force modulations, the force balance corresponding to harmonic FMM quasi-static vibration can be estimated as $k_1 A_{\text{FMM}} \approx k_{\text{eff}} \Delta d$ for an indentation amplitude $\Delta d = A_{\text{stiff}} - A_{\text{FMM}}$. Thus, a decrease (increase) in the measured value of A_{FMM} is expected on more compliant (stiffer) areas (see Fig. 1d).

The resulting FMM equation $k_{\text{eff}}/k_1 = 1/(A_{\text{stiff}}/A_{\text{FMM}} - 1)$, as clarified in eqn (1), relates the contrast in the vibration amplitude map $[A_{\text{stiff}} - A_{\text{FMM}}(\vec{r})]/A_{\text{FMM}}(\vec{r})$ to the ratio between the force constants of the cantilever and the tip–sample contact. This ratio depends on the mechanical properties of the sample and tip. This equation offers a straightforward interpretation of the mechanical properties of soft materials with flat surfaces. In systems with stiffness much lower than that of the tip and negligible roughness, $k_{\text{eff}} \approx \{6F_L E_{\text{sample}} / (1 - \nu_{\text{sample}})^2\}^2 R_{\text{tip}}^{1/3}$ is independent of the sample topography, and any deformation of the tip can be neglected. Consequently, contrast in the FMM images can be attributed almost exclusively to gradients in the mechanical properties of the sample, in particular, to variations of E_{sample} since the spatial dependence of ν_{sample} is smoother.

However, when the target surface is a metal or ceramic polycrystalline film grown by the Volmer–Weber (V–W) mechanism, interpreting the FMM images is a more complex task. These films are composed of grains with non-negligible roughness, which implies high curvature gradients. Ceramic and metal grains may also have stiffnesses comparable to that of the tip. Therefore, the sample topography and tip deformation become non-negligible factors, as we describe in the main text. Our procedure to remove the topography contribution from the FMM amplitude maps and inferred material properties of

the surface is related to other research studies³⁵ with similar aims, in particular with respect to features with sizes in the order of the tip radius.

Experimental. The FMM experiments were performed with a commercial AFM (Nanotec Electronica S.L.) in a dry $\text{N}_2(\text{g})$ atmosphere.³⁶ The environmental humidity was held below 10% in order to avoid capillary forces. The modulation voltage ΔV was applied to a piezoelectric element at the base of the cantilever. Si cantilevers (PPP-NCHR Nanosensors) with $k_1 = 40 \text{ N m}^{-1}$, $R_{\text{tip}} = 10 \text{ nm}$ and $f_{01} = 300 \text{ kHz}$ were used. Topographic images and FMM amplitude images were acquired simultaneously. In order to remain within the linear elastic regime of the material, the static load F_L and modulation voltage ΔV were chosen to produce indentations of only a few Å. The relationship between ΔV and ΔF for each experiment was estimated from the static and dynamic calibrations of the photodiode (namely, photodiode response in nm V^{-1} and signal gain at the modulation frequencies). Specifically, for the 600 nm and 1200 nm thick Au films, we obtain $F_L \pm \Delta F \approx 180[\text{nN}] \pm 131[\text{nN V}^{-1}] \times \Delta V[\text{V}]$ and $F_L \pm \Delta F \approx 200[\text{nN}] \pm 839[\text{nN V}^{-1}] \times \Delta V[\text{V}]$ respectively. The frequency-locked loop (FLL) fixed to the modulation frequencies ($f = 47 \text{ kHz}$ for 600 nm and 80.6 kHz for 1200 nm) allowed us to determine the harmonic indentation amplitude Δd with an experimental error of $\delta d = 0.2 \text{ Å}$, as shown in Fig. 1 for systems with low stiffness contrast. The FLL mode improves the FMM resolution by attenuating inelastic responses to the tip–sample interactions. Also, in FLL mode, FMM exhibits enhanced resolution on abrupt hollow features¹⁸ (e.g., GBs and steps at vicinal surfaces) where the effective radius R_{eff} of contact diverges for $\kappa(\vec{r}) \rightarrow -1/R_{\text{tip}}$. The data were processed assuming the following mechanical properties: $E_{\text{Au}} = 78 \text{ GPa}$ and $\nu_{\text{Au}} = 0.44$ for the sample, and $E_{\text{Si}} = 170 \text{ GPa}$ and $\nu_{\text{Si}} = 0.28$ for the tip material.

Bimodal AFM

Bimodal AFM is a nanomechanical spectroscopy method that enables simultaneous and accurate maps of material properties.^{23–26} The bimodal AFM measurements were performed with a Cypher S microscope (Asylum Research, Oxford Instruments) operating in the AM–FM configuration.^{23,24} We used Si cantilevers PPP-NCH (Nanosensors) characterized by $f_{01} = 293 \text{ kHz}$, $f_{02} = 1848 \text{ kHz}$, $R_{\text{tip}} = 2 \text{ nm}$, $k_1 = 40 \text{ N m}^{-1}$ and $k_2 = 2164 \text{ N m}^{-1}$.^{37–39} In the AM–FM configuration, the feedback acts on the amplitude of the first eigenmode and on the frequency shift of the resonant frequency of the second. Thus, the driving frequency of the first flexural mode f_{01} is fixed during imaging, while the oscillation amplitude A_1 is used as the feedback parameter to track the topography of the sample. In the second mode, changes in the resonant frequency Δf_{02} are recorded while imaging. The oscillation amplitude of the second mode A_2 is kept constant during this process. To keep track of changes in Δf_{02} over the surface, we keep the phase shift locked at 90° with a phase-locked loop (PLL). These feedback loops provide the experimental observables that are transformed into E_{eff} for the Hertz model, through analytical

expressions.²⁶ The images were taken at $A_{\text{sp}} = 10$ nm, with free amplitudes of $A_{01} = 20$ nm and $A_{02} = 0.4$ nm.

Acknowledgements

C. P. thanks P. Ares and I. Horcas for their help in resolving doubts about the FMM setup. Financial support was provided by the Ministerio de Economía y Competitividad (grants MAT2014-52477-C5-5-P to CP and EV; CSD2010-00024 and MAT2013-44858-R to RG) and by the European Research Council (grant ERC-AdG-340177, 3DNanoMech, to RG).

References

- 1 A. Witvrouw, H. A. C. Tilmans and I. De Wolf, *Microelectron. Eng.*, 2004, **76**, 245.
- 2 S. Kim, *J. Electrochem. Soc.*, 2011, **158**, H904.
- 3 J.-H. Cho, T. James and D. H. Gracias, *Adv. Mater.*, 2010, **22**, 2320.
- 4 L. B. Freund and S. Suresh, *Thin Film Materials: Stress, Defect Formation and Surface Evolution*, Cambridge University Press, Cambridge, England, 2003.
- 5 C. Friesen and C. V. Thompson, *Phys. Rev. Lett.*, 2004, **93**, 056104.
- 6 F. Spaepen, *Acta Mater.*, 2000, **48**, 31.
- 7 E. Chason, B. W. Sheldon, L. B. Freund, J. A. Floro and S. J. Hearne, *Phys. Rev. Lett.*, 2002, **88**, 156103.
- 8 R. Koch, D. Hu and A. K. Das, *Phys. Rev. Lett.*, 2005, **94**, 146101.
- 9 A. Gonzalez-Gonzalez, C. Polop and E. Vasco, *Phys. Rev. Lett.*, 2013, **110**, 056101.
- 10 H. Z. Yu and C. V. Thompson, *Appl. Phys. Lett.*, 2014, **194**, 141913.
- 11 B. Fu, W. An, C. H. Turner and G. B. Thompson, *Phys. Rev. Lett.*, 2010, **105**, 096101.
- 12 A. Saedi and M. J. Rost, *Nat. Commun.*, 2016, **7**, 10733.
- 13 A. Raman, S. Trigueros, A. Cartagena, A. P. Z. Stevenson, M. Susilo, E. Nauman and S. Antoranz Contera, *Nat. Nanotechnol.*, 2011, **6**, 809.
- 14 G. López-Polín, C. Gómez-Navarro, V. Parente, F. Guinea, M. I. Katsnelson, F. Pérez-Murano and J. Gómez-Herrero, *Nat. Phys.*, 2015, **11**, 26.
- 15 A. P. Perrino and R. Garcia, *Nanoscale*, 2016, **8**, 9151.
- 16 C. Polop, C. Rosiepen, S. Bleikamp, R. Drese, J. Mayer, A. Dimiyati and T. Michely, *New J. Phys.*, 2007, **9**, 74.
- 17 P. Maivald, H. J. Butt, S. A. C. Gould, C. B. Prater, B. Drake, J. A. Guriey, V. B. Elings and P. K. Hansma, *Nanotechnology*, 1991, **2**, 103.
- 18 F. B. Li, G. E. Thompson and R. C. Newman, *Appl. Surf. Sci.*, 1998, **126**, 21.
- 19 M. Radmacher, R. W. Tillmann and H. E. Gaub, *Biophys. J.*, 1993, **64**, 735.
- 20 X. Xu, M. Koslowski and A. Raman, *J. Appl. Phys.*, 2012, **111**, 54303.
- 21 R. Wagner and J. P. Killgore, *Appl. Phys. Lett.*, 2015, **107**, 203111.
- 22 The curvature of the rough surface of a sample was computed as follows:

$$\kappa(\vec{r}) = -\frac{[1 + \partial_x h(\vec{r})^2] \partial_y^2 h + [1 + \partial_y h(\vec{r})^2] \partial_x^2 h - 2 \cdot \partial_x h(\vec{r}) \cdot \partial_y h(\vec{r}) \cdot \partial_{xy} h(\vec{r})}{[1 + \partial_x h(\vec{r})^2 + \partial_y h(\vec{r})^2]^{3/2}},$$
 where $h(\vec{r})$ is an interpolation of the simultaneously imaged topography using Lagrange polynomials of degree 3. This choice ensures non-trivial and continuous second derivatives.
- 23 R. Garcia and E. T. Herruzo, *Nat. Nanotechnol.*, 2012, **7**, 217.
- 24 R. Garcia and R. Proksch, *Eur. Polym. J.*, 2013, **49**, 1897.
- 25 E. T. Herruzo, A. P. Perrino and R. Garcia, *Nat. Commun.*, 2014, **5**, 3126.
- 26 A. Labuda, M. Kocun, W. Meinhold, D. Walters and R. Proksch, *Beilstein J. Nanotechnol.*, 2016, **7**, 970.
- 27 H. Ogi, M. Fujii, N. Nakamura, T. Yasui and M. Hirao, *Phys. Rev. Lett.*, 2007, **98**, 195503.
- 28 W. M. C. Yang, T. Tsakalacos and J. E. Hillard, *J. Appl. Phys.*, 1977, **48**, 876.
- 29 Finite Element Modeling (FEM) simulations were performed with COMSOL Multiphysics 5.2. We designed a two-step solid mechanics study: the first step concerns the pre-stressed stage of the central grain, and the second step approximates the mechanical response of the pre-stressed grain to the load exerted by a conical Si tip with a spherical apex. The simulation geometry and the distribution of the contact pressure are included in the ESI.†
- 30 The σ -dependence of E_{eff} due to the lattice anharmonicity effect was estimated from the data in Table 1 of ref. 27. In the case of polycrystalline Au films (with $\langle 111 \rangle$ Au/ z -axis), the anharmonic effect was estimated to be $(\partial E_z / \partial S_x) / E_z = 4.53$, with the in-plane strain being $S_x = S_y = (1 - \nu) \sigma / E_{x-y}$. Here $\sigma = \sigma_x = \sigma_y$ is the biaxial residual stress, and the Young's modulus is $E_{x-y} = E_z$ for $\sigma = 0$.
- 31 $\beta = 4$ for an equibiaxial stress field with $\sigma = |\sigma_x| = |\sigma_y|$, and $\beta = 2\pi$ for an isotropic stress field with $\sigma = \sigma(r)$.
- 32 A. González-González, J. L. Sacedón, C. Polop, E. Rodríguez-Canas, J. A. Aznarez and E. Vasco, *J. Vac. Sci. Technol., A*, 2009, **27**, 1012.
- 33 The stress variation in regions near a GB has the same order of magnitude as the mechanical strengths of many pure metals and alloys. For example, the representative ultimate strengths of Au, Ag, Fe, Ta, Ti, Sn, Cu, Al, and Zn alloys are all in the range of 100–500 MPa.
- 34 H.-C. Chiu, S. Kim, C. Klinke and E. Riedo, *Appl. Phys. Lett.*, 2012, **101**, 103109.
- 35 M. Stark, C. Möller, D. J. Müller and R. Guckenberger, *Biophys. J.*, 2001, **80**, 3009.
- 36 I. Horcas, R. Fernández, J. M. Gómez-Rodríguez, J. Colchero, J. Gómez-Herrero and A. M. Baró, *Rev. Sci. Instrum.*, 2007, **78**, 013705.
- 37 H. J. Butt and M. Jaschke, *Nanotechnol.*, 1995, **6**, 1.
- 38 J. R. Lozano, D. Kiracofe, J. Melcher, R. García and A. Raman, *Nanotechnol.*, 2010, **21**, 465502.
- 39 A. Labuda, M. Kocun, M. Lysy, T. Walsh, J. Meinhold, T. Proksch, W. Meinhold, C. Anderson and R. Proksch, *Rev. Sci. Instrum.*, 2016, **87**, 73705.